Half-minute-scale atomic coherence and high relative stability in a tweezer clock

https://doi.org/10.1038/s41586-020-3009-y

Received: 18 June 2020

Accepted: 17 September 2020

Published online: 16 December 2020

Check for updates

Aaron W. Young[1,2], William J. Eckner[1,2], William R. Milner[1,2], Dhruv Kedar[1,2], Matthew A. Norcia[1,2], Eric Oelker[1,2], Nathan Schine[1,2], Jun Ye[1,2] & Adam M. Kaufman[1,2]✉

The preparation of large, low-entropy, highly coherent ensembles of identical quantum systems is fundamental for many studies in quantum metrology[1], simulation[2] and information[3]. However, the simultaneous realization of these properties remains a central challenge in quantum science across atomic and condensed-matter systems[2,4–7]. Here we leverage the favourable properties of tweezer-trapped alkaline-earth (strontium-88) atoms[8–10], and introduce a hybrid approach to tailoring optical potentials that balances scalability, high-fidelity state preparation, site-resolved readout and preservation of atomic coherence. With this approach, we achieve trapping and optical-clock excited-state lifetimes exceeding 40 seconds in ensembles of approximately 150 atoms. This leads to half-minute-scale atomic coherence on an optical-clock transition, corresponding to quality factors well in excess of 10^{16}. These coherence times and atom numbers reduce the effect of quantum projection noise to a level that is comparable with that of leading atomic systems, which use optical lattices to interrogate many thousands of atoms in parallel[11,12]. The result is a relative fractional frequency stability of $5.2(3)\times10^{-17}\tau^{-1/2}$ (where τ is the averaging time in seconds) for synchronous clock comparisons between sub-ensembles within the tweezer array. When further combined with the microscopic control and readout that are available in this system, these results pave the way towards long-lived engineered entanglement on an optical-clock transition[13] in tailored atom arrays.

A key requirement in quantum metrology, simulation and information is the control and preservation of coherence in large ensembles of effective quantum two-level systems, or qubits[1–3]. One way to realize these features is with neutral atoms[4,14], which benefit from being inherently identical and having weak and short-range interactions in their ground states. This, combined with the precise motional and configurational control provided by tailored optical potentials, enables assembly of large ensembles of atomic qubits[15–18] without the need for careful calibration of individual qubits or additional shielding from uncontrolled interactions with the environment. As a result, groundbreaking work has been done in such systems using alkali atoms, including the realization of controllable interactions and gates[19,20], preparation of useful quantum resources[21] and simulation of various spin models of interest[22,23]. These techniques have recently been extended to alkaline-earth (or alkaline-earth-like) atoms[8–10,24], which further provide access to extremely long-lived nuclear and electronic excited states, as well as new schemes for Rydberg spectroscopy[25].

These recent advancements have enabled the development of tweezer array optical clocks[5,6], which leverage the flexible potentials provided by optical tweezer arrays to rapidly prepare and interrogate ensembles of many non-interacting atoms. As a result, these clocks can balance the pristine isolation and high duty cycles available in single-ion-based optical clocks[26,27] with the large ensembles and resultant low quantum projection noise (QPN) available in optical lattice clocks[1,11,12,28]. The most stable tweezer clock demonstrated so far used a one-dimensional (1D) array containing five atoms, and consequently was limited by QPN to a stability of $4.7\times10^{-16}\tau^{-1/2}$ (ref. [6]), about an order of magnitude worse than current state-of-the-art values of $3.1\times10^{-17}\tau^{-1/2}$, reported for synchronous comparisons in a three-dimensional (3D) lattice clock[11], and $4.8\times10^{-17}\tau^{-1/2}$, for a comparison between two clocks[12]. Extending tweezer array clocks to large two-dimensional (2D) arrays helps to close this gap by increasing the atom number while maintaining the high duty cycles achievable in tweezer-based systems[6].

The tweezer clock architecture also benefits from microscopic single-particle control through 100-nm-precision positioning of individual atoms. Such control can help to probe and protect against the mechanisms that influence quantum coherence in neutral atom clocks, such as interactions, tunnelling and spontaneous emission[7]. This capability, combined with a series of other advances, allows us to realize sub-hertz control of an optical-clock transition in a tweezer array of 320 traps containing a total of ~150 atoms on average (see Fig. 1a, b). We demonstrate the ability to load ground-state cooled atoms into shallow tweezers that are at a 'magic' wavelength for the clock transition, achieving excited-state lifetimes of up to 46(5) s and clock frequency homogeneity on the scale of tens of millihertz across all tweezers

[1]JILA, University of Colorado and National Institute of Standards and Technology, Boulder, CO, USA. [2]Department of Physics, University of Colorado, Boulder, CO, USA.
✉e-mail: adam.kaufman@colorado.edu

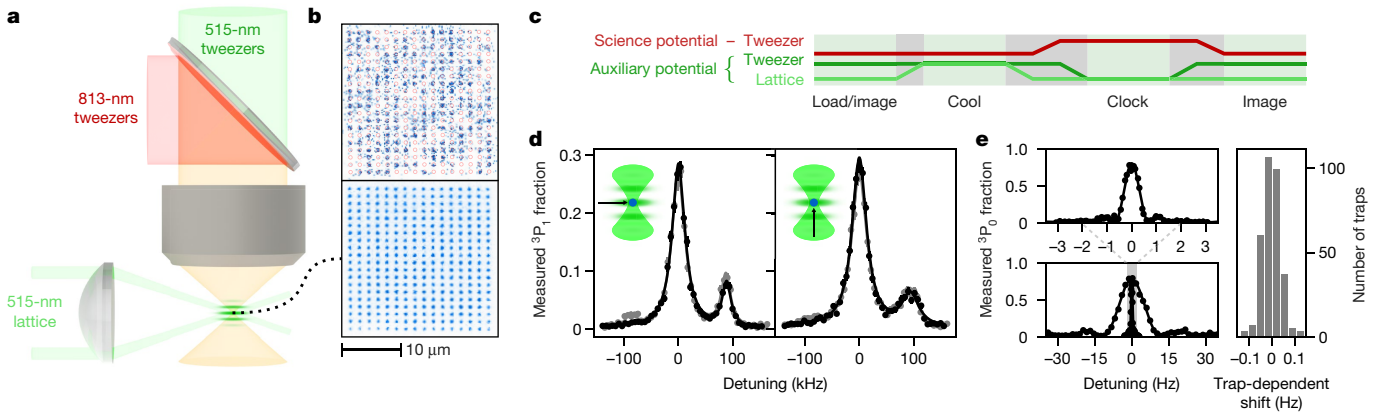

Fig. 1 | 3D ground-state cooled strontium atoms in a 320-site magic-wavelength tweezer array. a, To generate large numbers of traps that are compatible with ground-state cooling and narrow-line spectroscopy, we combine a shallow 'science' potential at 813 nm, which is a magic wavelength for the clock transition, with a tightly confining 'auxiliary' potential at 515 nm, which includes both a tweezer array and a crossed-beam optical lattice to provide tight confinement along all spatial axes. **b**, Representative single-shot (top) and averaged (bottom) images of atoms demonstrate site-resolved readout of a 16 × 20 array of tweezers, with a spacing of 1.2 μm (1.5 μm) in the vertical (horizontal) direction. The red circles in the single-shot image denote the tweezer positions to guide the eye. **c**, In a typical experimental sequence, these potentials cooperate to prepare and read out 3D ground-state cooled atoms in traps that are compatible with narrow-line clock spectroscopy. **d**, To confirm that the atoms in the science potential are appropriately cooled, we perform sideband spectroscopy after cooling in the auxiliary potential (black points) and after adiabatically transferring the atoms to and back from the science potential (grey points; see main text for details). Each point in this plot is averaged over 20 trials and over all 320 tweezers in the array. The insets indicate the orientation of the probe beam relative to the traps, showing probes in the radial direction (left) and in the axial direction (right). **e**, With atoms trapped in the science potential, array-averaged Rabi spectroscopy of the $^1S_0 \leftrightarrow {}^3P_0$ clock transition provides Fourier-limited linewidths of 10.1(2) Hz and 0.62(1) Hz (full-width at half-maximum), in good agreement with the expected sinc lineshapes based on the known probe durations used in each case (solid lines). The callout (top) shows the Fourier-limited 0.6-Hz feature in detail, with no reduction in the maximal transfer fraction compared to the 10-Hz case. Each point in these plots is averaged over 24 trials and over all tweezers. Error bars (see Methods section 'Units and errors') are smaller than the point size. We investigate the presence of inhomogeneous, trap-dependent shifts of the clock transition by independently fitting the centres of the spectra associated with each tweezer, which vary with a standard deviation of 0.039(2) Hz (right).

(for the definition of uncertainties, see Methods sections 'Units and errors' and 'Clock interrogation'). As a consequence, we measure a coherence time of 19.5(8) s for synchronous frequency comparisons involving the entire array, and observe evidence of atomic coherence out to 48(8) s for select atoms in the array, corresponding to an atomic quality factor of $Q = 6.5(1.1) \times 10^{16}$. These characteristics reduce the effects of QPN in the tweezer clock platform to a level that is on par with the state of the art[11,12], yielding a relative fractional frequency stability of $5.2(3) \times 10^{-17}\tau^{-1/2}$ for synchronous self-comparisons.

A central challenge for using tweezer array systems in quantum science is maintaining control while scaling to larger atom numbers, because the required optical power scales linearly with the system size. Our solution is to use several optical potentials optimized for different stages of the experiment, and to realize state-preserving, low-loss transfer between these different potentials[29]. We use an 'auxiliary' potential composed of both a tweezer array and an optical lattice for initial state preparation and readout, and a 'science' potential for clock interrogation, which is composed of a tweezer array that is at a magic wavelength for the clock transition (see Fig. 1a, c). The auxiliary potential efficiently generates many deep traps that allow high-fidelity ground-state cooling of large ensembles of atoms. By pre-cooling the atoms, the power requirements on the science potential are greatly relaxed and no longer pose a limitation on atom number or state preparation.

To confirm that the atoms remain cold when transferring them between these potentials, we perform sideband thermometry[9], first in the auxiliary potential (including the lattice) immediately after sideband cooling, and then after adiabatically passing the atoms to the science potential, holding for 25 ms, and passing them back (see Methods and Extended Data Figs. 1, 3). With optimal alignment, this whole 'handoff' procedure can be performed with 0.0(3)% additional atom loss (see Methods). As shown in Fig. 1d, before the handoff we observe an average phonon occupation of $\bar{n} = 0.07^{+0.14}_{-0.07}$, $0.06^{+0.08}_{-0.06}$ and 0.07 ± 0.06 in the axial, first radial and second radial directions, respectively. After the handoff, these occupations are $\bar{n} = 0.25 \pm 0.12$, 0.31 ± 0.13 and 0.27 ± 0.10, correspondingly. Because we expect that heating occurs during both steps of the handoff, the mean of these two measurements serves as an estimate of the temperature of the atoms in the science potential. In a smaller 6 × 6 region at the centre of the array the axial cooling and handoff performance is vastly improved, with an average phonon occupation of $\bar{n} = 0.00^{+0.06}_{-0.00}$ ($\bar{n} = 0.06^{+0.10}_{-0.06}$) before (after) the handoff (see Methods and Extended Data Fig. 1).

These low temperatures enable clock operation in shallow tweezers, which both improves scalability and minimizes clock decoherence due to Raman transitions driven by the trap photons[7,30]. Specifically, in tweezers of $25E_r$ (or 4.3 μK) depth (where E_r is the recoil energy associated with a single 813-nm photon)—barely a quarter of the shallowest depths reported in previous works[6]—we observe trap lifetimes of 160(10) s (Fig. 2a), probably limited by our vacuum. At this depth, we measure Fourier-limited spectroscopic features on the $^1S_0 \leftrightarrow {}^3P_0$ optical-clock transition with linewidths as low as 0.62(1) Hz (full-width at half-maximum) averaged across all tweezers, with inhomogeneous broadening on the scale of tens of millihertz (Fig. 1e; see Methods).

Unlike in lattice clocks, where the effects of tunnelling can become limiting at depths below ~$30E_r$ along a single axis (~$100E_r$ in a 3D lattice)[7], we observe no evidence of tunnelling or thermal hopping in tweezers as shallow as $6E_r$ (see Methods). Importantly, at this depth we calculate the tunnelling rate to be ~1 Hz, suggesting that disorder also has a key role in pinning the atoms. Although this is encouraging, at these depths other sources of atom loss (see Methods) begin to limit our trap lifetime to far below 160(10) s. A competition between these losses and Raman scattering leads to an optimal trap depth, with respect to the clock state lifetime, of ~$14E_r$, where we measure a lifetime of 46(5) s (Fig. 2a). This lifetime is in good agreement with the predicted value of 44(6) s based on the measured ground-state trap lifetime of 96(8) s, and the expected contributions from trap-induced Raman scattering and black-body radiation[7,30].

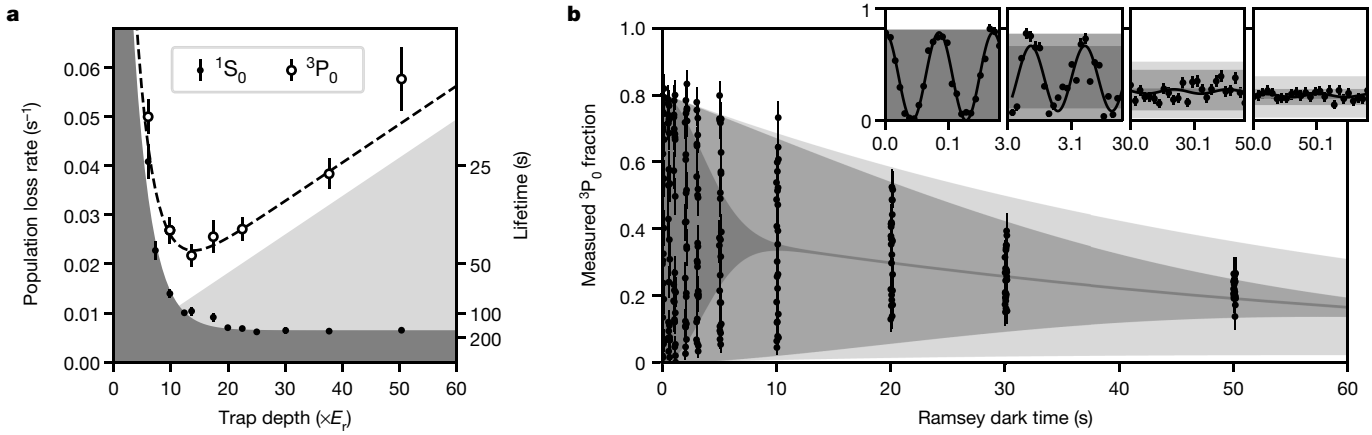

Fig. 2 | Minute-scale atomic lifetime and ensemble coherence studies. **a**, To determine limits on atomic coherence, we measure the lifetime of both the ground ($^1S_0$; black points) and clock ($^3P_0$; black circles) states. The ground-state lifetimes are inferred from exponential fits to the measured population of atoms as a function of time, using 20 or more runs of the experiment and averaging over all tweezers. The clock-state lifetimes are inferred from two such datasets with and without repumping (see Methods). For ground-state atoms, the lifetime saturates to 160(10) s in deep traps, with additional technical sources of atom loss contributing in shallower traps (exponential fit to $^1S_0$ data; dark grey). For clock-state atoms, an optimal trap depth arises from a competition between this atom loss, which prefers deep traps, and depumping via spontaneous Raman scattering of the trap light (theory prediction with no free parameters; light grey)[7,30] (see Methods), which prefers shallow traps. The combination of these loss mechanisms (dashed line) is in good agreement with the measured clock-state lifetimes, including the optimum of 46(5) s at $14E_r$. **b**, For clock operation, we perform Ramsey spectroscopy in $15E_r$-deep tweezers (black points), near this optimal depth. Given the measured clock-state lifetime, we would expect the contrast to decay with an exponential time constant of 55(8) s (light-grey region). However, we expect tweezer-dependent light shifts to result in Gaussian decay with a time constant of 33(1) s at $15E_r$ (ref. [6]; see Methods and Supplementary Information). The combination of these two effects is denoted by the medium-grey region. We note that each data point corresponds to an average over all 320 tweezers in a single shot of the experiment. As a result, although the atom–laser coherence decays over 3.6(2) s (dark-grey region) (see Methods and Extended Data Fig. 4), the variance of the Ramsey signal decays on a timescale set by atomic coherence. This is clarified by the insets, which share units with the main axes and show detailed views of Ramsey evolution at different times. Here, it is possible to see the initial loss of phase coherence with the laser, followed by total loss of coherence (and thus variance in this signal) in the system.

Our measured lifetimes suggest that at $15E_r$, the Ramsey contrast should decay exponentially with a time constant of 55(8) s. In practice, this decay is exacerbated by tweezer-induced frequency shifts associated with slight variations in the trapping wavelength between tweezers[5,6]. The result is Gaussian decay with an expected time constant of 33(1) s (see Methods and Supplementary Information). In our measurements, the signal at each Ramsey time is a single-shot measurement such that, even though atom–laser coherence decays over ~3 s (see Methods and Extended Data Fig. 4), we can infer the atomic coherence from the variance of this signal, which remains high on much longer timescales (Fig. 2b; see Methods and Supplementary Information). The atomic coherence, and thus the Ramsey contrast, inferred from this measurement decays with a 1/e time of 19.5(8) s (Fig. 2b), slightly faster than the prediction based on the measured lifetime and dephasing. This corresponds to an effective quality factor of $Q = 1.9(1) \times 10^{16}$, which is limited by inhomogeneous broadening.

Even in the absence of atom–laser coherence, we can perform a synchronous clock comparison that takes advantage of this long-lived atomic coherence by comparing the relative phase between two sub-ensembles in the tweezer array[5,31,32]. Because readout occurs in a site-resolved manner, the partitioning of these ensembles can be chosen arbitrarily. Specifically, we choose a 'checkerboard' partitioning that yields no net tweezer-induced frequency shift between the two sub-ensembles, and a 'diagonal' partitioning that yields a near-maximal frequency shift (Fig. 3a insets). At Ramsey dark times that exceed the atom–laser coherence time, the Ramsey phase is randomized. As a result, parametric plots of the excitation fraction in the two sub-ensembles result in points that randomly fall along the edge of an ellipse, where the size of the ellipse is related to the average atomic coherence, and the opening angle of the ellipse is related to the net phase (and thus frequency) shift between sub-ensembles (Fig. 3a). Extracting a phase from these distributions via ellipse fitting, particularly in the presence of QPN, yields biased results near zero phase or contrast[32,33]. Whereas this means that any useful measurement must operate away from this point, to initially identify an optimal Ramsey time with respect to relative stability we choose to operate in a biased regime with no phase offset. This is because any partitioning that yields a frequency shift results in a phase offset, and thus bias, that varies with Ramsey time, obscuring the optimal value. We characterize this biasing via Monte Carlo simulations (see Supplementary Information) which, when combined with the expected effects of QPN, are in good agreement with the data (Fig. 3b).

Guided by these measurements, we perform a 4.3-h-long synchronous comparison between sub-ensembles at the near-optimal Ramsey time of 15 s. At 15 s, the diagonal partitioning results in a sufficiently large tweezer-induced phase shift between sub-ensembles to eliminate the effects of biasing (Fig. 3b, c). This is confirmed both by the above-mentioned Monte Carlo simulations used to characterize bias and by the agreement between the data and a prediction based exclusively on QPN. Specifically, we expect a tweezer-induced frequency offset of 7.0(1.3) mHz on the basis of previous measurements of the light shift[6,34], and measure an offset of 7.15(18) mHz. The uncertainty in this measurement corresponds to a fractional frequency precision of 4.2×10^{-19}. In this unbiased condition, we compute the Allan deviation (see Supplementary Information), which averages down with a slope of $5.2(3) \times 10^{-17}\tau^{-1/2}$. This is in good agreement with the expected value of $5.2 \times 10^{-17}\tau^{-1/2}$ from QPN with no bias correction (Fig. 3c) and comparable to the state-of-the-art value of $3.1 \times 10^{-17}\tau^{-1/2}$ for such synchronous comparisons reported in leading 3D lattice clocks[11]. Moreover, the long interrogation times used here allow us to match the highest duty cycles achieved in our previous work of 96%[6], even without performing repeated interrogation. As a result, although not demonstrated here, Dick effect noise is not expected to substantially affect the stability of an asynchronous comparison[6].

To better understand the limitations of this system, we study atomic coherence within the array using the single-site observables afforded

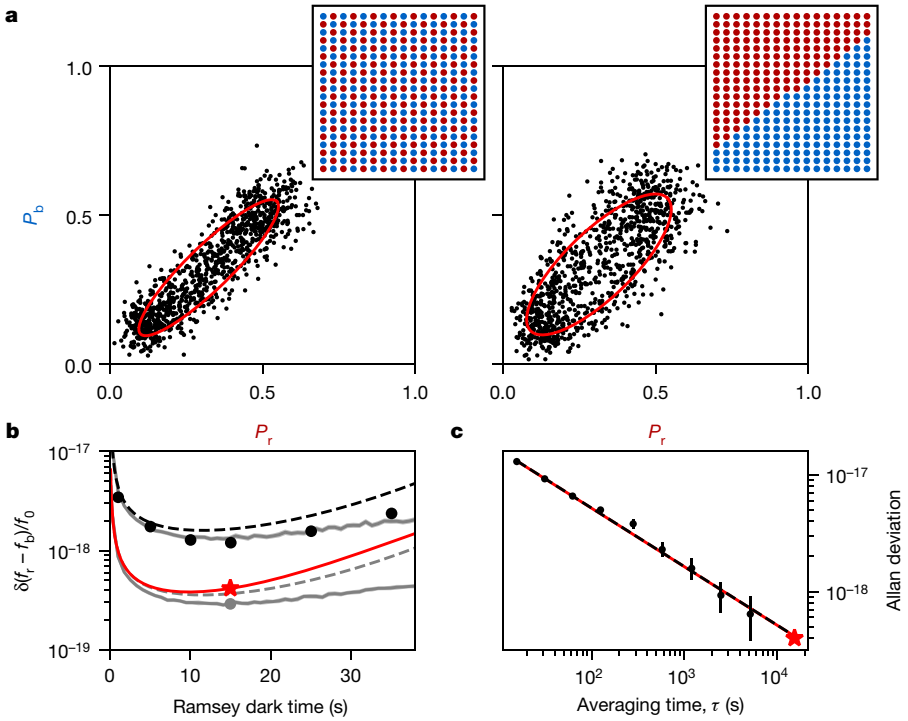

Fig. 3 | Resolving millihertz shifts of an optical transition. a, We perform a synchronous clock comparison by partitioning the array into two sub-ensembles (insets, red and blue) and creating a parametric plot of the $^3P_0$ excited-state fraction in the blue ensemble (P_b) versus in the red ensemble (P_r), where each point corresponds to a single shot of the experiment (in this case at a 15-s interrogation time in $15E_r$-deep tweezers). In the checkerboard (left) partitioning there is no mean frequency shift between the two sub-ensembles, whereas in the diagonal (right) case we expect a shift of 7.0(1.3) mHz (see Methods and Supplementary Information). The relative frequency between the sub-ensembles can be extracted via ellipse fitting (red lines), which in the diagonal case yields 7.15(18) mHz. We note that such fits are biased near zero phase shift, as is evident in the fit to the checkerboard ensemble, which returns an artificially large phase shift. **b**, To identify an optimal Ramsey dark time, we compute the fractional frequency uncertainty between the sub-ensembles as a function of Ramsey time at fixed total averaging time (see Supplementary Information). The black points (grey point) correspond(s) to 13 min (4.3 h) of averaging and are extracted from the checkerboard partitioning. We note that, owing to biasing, these values are not representative of a true stability. This is made clear by the dashed curves, which correspond to the expected QPN, and the solid grey curves, which include an additional correction factor calculated via Monte Carlo simulations to account for the biased fits (shaded regions denote 1-s.d. confidence interval) (see Supplementary Information). At interrogation times of 15 s, the diagonally separated sub-ensembles have a sufficient phase shift to remove the bias in the fits. This condition (red star) shows the fractional frequency uncertainty of the full 4.3-h-long measurement, with a value of 4.2×10^{-19}. This is in good agreement with the expected QPN limit with no bias correction (red curve). **c**, We can further compute an Allan deviation associated with this measurement (black points), which averages down with a slope of $5.2(3) \times 10^{-17}\tau^{-1/2}$ (black dashed line). This is in good agreement with the expected value of $5.2 \times 10^{-17}\tau^{-1/2}$ from the QPN (red line). The red star is duplicated here as a point of comparison (we note that this point is not strictly an Allan deviation, and is extracted via jackknifing) (see Supplementary Information).

by our microscope, and look for classical correlations in the states of the atoms after Ramsey evolution. Specifically, we compute the $g^{(2)}$ correlator (see Supplementary Information) between atoms in different tweezers as a function of Ramsey dark time and relative tweezer position $\Delta\mathbf{r}$, which we denote as $C(\Delta\mathbf{r})$ (Fig. 4a)[35–37]. After averaging over the phase of the laser, for two atoms 1 and 2, each with density matrix ρ_j ($j = 1, 2$), the correlator is equal to $2A_1A_2\cos(\phi_1 - \phi_2)$, where A_j and ϕ_j are the amplitude and phase of the off-diagonal elements of the density matrix for atom j, $\rho_{\mathrm{eg},j} = A_j e^{i\phi_j}$. This quantity serves as a site-resolved measure of tweezer-induced clock transition shifts[35–37] (see Supplementary Information), revealing that along the forward diagonal of the array, where frequency offsets between tweezers—and thus clock frequency offsets—are maximal, the atoms become uncorrelated and eventually develop negative correlations. Along the anti-diagonal, where there is no frequency offset between tweezers, positive correlations persist over much longer timescales. We further observe the development of fringes in the correlator along the more tightly spaced axis of the array, which we hypothesize are the result of overlaps between tweezers (see Supplementary Information).

The coherence of a given atom, $|\rho_{\mathrm{eg}}|$, may be defined with respect to a partner atom, or an ensemble of atoms, which serves as a phase reference[32,36,38]. If the atom and reference are at the same frequency, any excess decay of correlations between the atom and reference compared to the decay of the reference can be attributed to loss of single-atom coherence (see Supplementary Information); if the frequencies are different, the signal falls more rapidly owing to the evolving phase difference and constitutes a lower bound on the single-atom coherence time. Hence, we can compare the average correlations between one atom and the total spin projection of the remaining array, C_A, with the measured Ramsey contrast (Fig. 4b). By applying this procedure to the atoms in the central 4×4 sites, which have a clock frequency similar to that of the array mean, we infer a single-atom 1/e coherence time of 48(8) s and a resulting atomic oscillator quality factor of $Q = 6.5(1.1) \times 10^{16}$ (Fig. 4c). This is comparable to the expected value of 55(8) s, and corresponds to the useable timescale for frequency comparison measurements (as in Fig. 3) that we would expect if all tweezers were at the same wavelength, as might be achieved with the use of a spatial light modulator.

To extend this argument to each atom in the array, particularly to those with clock frequencies that differ substantially from the ensemble mean, we can simply choose a phase reference that has a similar frequency to the atom under measurement. Specifically, we consider 2×2 sub-ensembles of the array, for which we expect tweezer-induced

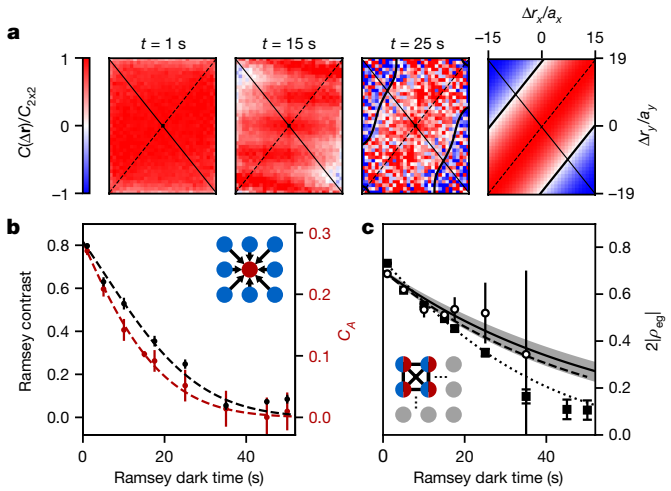

Fig. 4 | Microscopic studies of atomic coherence. a, As a measure of atomic coherence, we compute the spatially resolved atom–atom correlation function, $C(\Delta\mathbf{r})$ (see Supplementary Information), as a function of Ramsey dark time. These plots are normalized by $C_{2\times2}$, as defined below, to isolate the effects of dephasing from atom loss and decay. The relative displacements Δr_x, Δr_y are normalized by the array spacing in the relevant direction ($a_x = 1.5\,\mu$m, $a_y = 1.2\,\mu$m) so that the pixel spacing corresponds to the tweezer spacing. Solid (dashed) diagonal lines indicate axes along which the tweezer wavelengths change (remain constant), showing accelerated (reduced) dephasing along the forward (reverse) diagonal of the array due to tweezer-induced frequency shifts (solid contours show where the correlator passes through zero). The rightmost panel shows a theoretical prediction at 25 s given our known tweezer frequencies and depths. We note that in these and the following plots, the statistics at different dark times vary between 22 and 990 trials, as is reflected in the size of the corresponding error bars. **b**, The coherence of a single atom (red circle in inset) can be measured by computing the average correlations C_A between the atom and an ensemble of reference atoms (blue circles). In this case, the reference ensemble is the entire array, and the excess decay of C_A (red points; averaged over a 4 × 4 block of atoms at the centre of the array) compared to the decay of the Ramsey contrast (black points) can be used to quantify the single-atom coherence time. Fits to these quantities (dashed lines) with a Gaussian and an exponential component yield overall 1/e times of 14.6(7) s and 19.5(8) s, respectively. **c**, On the basis of these measurements, we can infer a single-atom coherence time of 48(8) s (dashed line) (see Supplementary Information), which is in good agreement with a model based on the measured lifetimes and initial Ramsey contrast (solid line, error in grey). Open circles are C_A with the contribution to decay associated with the reference ensemble removed, which serves as a direct measurement of the single-atom coherence $|\rho_{eg}|$. In the absence of dephasing, an ensemble of these atoms would have a Ramsey contrast of $2|\rho_{eg}|$ (see Supplementary Information). To extend this measurement from the central 4 × 4 region to the full array, we consider the average correlation between all atom pairs in a 2 × 2 block averaged over all such blocks, $C_{2\times2}$. In this case, each atom in the block acts as a reference for all other atoms in the block (see inset). The square root of this quantity (black squares) decays with a fitted 1/e time of 33(2) s (short-dashed line), and serves as a lower bound on the average atomic coherence across the entire array (see Supplementary Information).

dephasing to be suppressed to a timescale of several hundred seconds. In this case, the sub-ensemble-averaged single-atom coherence can be written in terms of the average of the pairwise correlators (see Supplementary Information). With reasonable assumptions (see Supplementary Information), the square root of this quantity averaged across all such sub-ensembles contained in the array, $\sqrt{C_{2\times2}}$, provides a lower bound on the average atomic coherence $|\overline{\rho}_{eg}|$ of all ~150 atoms in the array. This bound has a measured 1/e lifetime of 33(2) s (Fig. 4c).

These coherence times and atom numbers have advanced the state of the art in atomic coherence at optical frequencies, and pushed tweezer clocks to an improved regime of relative stability. This is accomplished via a recipe for creating tailored optical potentials that results in a substantial increase in accessible sample sizes to hundreds of tweezers in this work, and presents a clear path towards scaling to more than a thousand tweezers (see Methods and Supplementary Information).

The advances in this work are, in part, guided by groundbreaking studies in optical lattice clocks[7], and might also illuminate new paths forward for these lattice systems that benefit from greater atom number than tweezer clocks. Although the elimination of tunnelling in this study is partially due to increased trap separation in comparison to lattice clocks, a far greater effect is the presence of disorder. Specifically, as is well known in tweezer systems[39,40], tweezer-to-tweezer disorder is hard to suppress on the energy scale of the tunnelling. Whereas this is a challenge for their use in Hubbard physics, here it serves to suppress tunnelling and prolong atomic coherence. This suggests that, in the context of lattice clocks, the use of a weak disordering potential superimposed on a standard optical lattice clock could enhance coherence time, which might be an alternative solution to directly modulating the tunnelling[7]. This highlights another important role for the tweezer clock: it serves as a clean, versatile platform for studying neutral-atom optical clocks and the mechanisms that influence their performance. In future accuracy studies (see Methods), the lack of interactions and itinerance in this system will ease dissection of coupled systematic effects.

Our work here lays a firm foundation for engineering entanglement on an optical-clock transition[13,41]. The large 2D arrays and tight spacings used here are key for future studies involving limited-range Rydberg interactions, providing access to larger samples with higher connectivity, stronger interactions and correspondingly greater entanglement. Furthermore, incremental upgrades to our existing setup (see Methods and Supplementary Information) will improve purity in state preparation by reducing imaging losses[6,8,9,42] and allowing higher-fidelity clock rotations, which will be key to implementing protocols to generate entanglement[13,21,43]. Although many-body entanglement scales exponentially poorly with single-particle decoherence, the coherence times reported here establish the prospect of a metrologically useful entangled optical clock operating with tens of atoms and seconds-long interrogation times. Our use of ^{88}Sr, which has a clock linewidth that is tunable with a magnetic field, also establishes longer-term directions for quantum metrology that are not fundamentally limited by spontaneous emission[44]. The microscopic control available in this system further opens the possibility of probing and verifying entanglement with microscopic observables and, in the context of quantum simulation, implementing various 2D spin models of interest[45–47]. For quantum information applications, such a system can also be used to perform Rydberg-mediated quantum gates on long-lived spin or optical qubits[19,20,24], or to prepare cluster states in a highly parallelized way for use in measurement-based quantum computing[48].

Online content

Any methods, additional references, Nature Research reporting summaries, source data, extended data, supplementary information, acknowledgements, peer review information; details of author contributions and competing interests; and statements of data and code availability are available at https://doi.org/10.1038/s41586-020-3009-y.

1. Ludlow, A. D., Boyd, M. M., Ye, J., Peik, E. & Schmidt, P. O. Optical atomic clocks. *Rev. Mod. Phys.* **87**, 637–701 (2015).
2. Georgescu, I. M., Ashhab, S. & Nori, F. Quantum simulation. *Rev. Mod. Phys.* **86**, 153–185 (2014).
3. Preskill, J. Quantum computing and the entanglement frontier. Preprint at https://arxiv.org/abs/1203.5813 (2012).
4. Saffman, M., Walker, T. G. & Molmer, K. Quantum information with Rydberg atoms. *Rev. Mod. Phys.* **82**, 2313–2363 (2010).
5. Madjarov, I. S. et al. An atomic-array optical clock with single-atom readout. *Phys. Rev. X* **9**, 041052 (2019).
6. Norcia, M. A. et al. Seconds-scale coherence on an optical clock transition in a tweezer array. *Science* **366**, 93–97 (2019).

7. Hutson, R. B., Goban, A., Marti, G. E. & Ye, J. Engineering quantum states of matter for atomic clocks in shallow optical lattices. *Phys. Rev. Lett*. **123**, 123401 (2019).
8. Cooper, A. et al. Alkaline-earth atoms in optical tweezers. *Phys. Rev. X* **8**, 041055 (2018).
9. Norcia, M. A., Young, A. W. & Kaufman, A. M. Microscopic control and detection of ultracold strontium in optical-tweezer arrays. *Phys. Rev. X* **8**, 041054 (2018).
10. Saskin, S., Wilson, J. T., Grinkemeyer, B. & Thompson, J. D. Narrow-line cooling and imaging of ytterbium atoms in an optical tweezer array. *Phys. Rev. Lett*. **122**, 143002 (2019).
11. Campbell, S. L. et al. A Fermi-degenerate three-dimensional optical lattice clock. *Science* **358**, 90–94 (2017).
12. Oelker, E. et al. Demonstration of 4.8×10^{-17} stability at 1 s for two independent optical clocks. *Nat. Photon*. **13**, 714–719 (2019).
13. Gil, L. I. R., Mukherjee, R., Bridge, E. M., Jones, M. P. A. & Pohl, T. Spin squeezing in a Rydberg lattice clock. *Phys. Rev. Lett*. **112**, 103601 (2014).
14. Browaeys, A. & Lahaye, T. Many-body physics with individually controlled Rydberg atoms. *Nat. Phys*. **16**, 132–142 (2020).
15. Barredo, D., de Léséleuc, S., Lienhard, V., Lahaye, T. & Browaeys, A. An atom-by-atom assembler of defect-free arbitrary two-dimensional atomic arrays. *Science* **354**, 1021–1023 (2016).
16. Endres, M. et al. Atom-by-atom assembly of defect-free one-dimensional cold atom arrays. *Science* **354**, 1024–1027 (2016).
17. Kumar, A., Wu, T.-Y., Giraldo, F. & Weiss, D. S. Sorting ultracold atoms in a three-dimensional optical lattice in a realization of Maxwell's demon. *Nature* **561**, 83–87 (2018).
18. Brown, M. O., Thiele, T., Kiehl, C., Hsu, T.-W. & Regal, C. A. Gray-molasses optical-tweezer loading: controlling collisions for scaling atom-array assembly. *Phys. Rev. X* **9**, 011057 (2019).
19. Levine, H. et al. Parallel implementation of high-fidelity multiqubit gates with neutral atoms. *Phys. Rev. Lett*. **123**, 170503 (2019).
20. Graham, T. M. et al. Rydberg-mediated entanglement in a two-dimensional neutral atom qubit array. *Phys. Rev. Lett*. **123**, 230501 (2019).
21. Omran, A. et al. Generation and manipulation of Schrödinger cat states in Rydberg atom arrays. *Science* **365**, 570–574 (2019).
22. Bernien, H. et al. Probing many-body dynamics on a 51-atom quantum simulator. *Nature* **551**, 579–584 (2017).
23. de Léséleuc, S. et al. Observation of a symmetry-protected topological phase of interacting bosons with Rydberg atoms. *Science* **365**, 775–780 (2019).
24. Madjarov, I. S. et al. High-fidelity entanglement and detection of alkaline-earth Rydberg atoms *Nat. Phys*. **16**, 857–861 (2020).
25. Wilson, J. et al. Trapped arrays of alkaline earth Rydberg atoms in optical tweezers. Preprint at https://arxiv.org/abs/1912.08754 (2019).
26. Chou, C. W., Hume, D. B., Koelemeij, J. C. J., Wineland, D. J. & Rosenband, T. Frequency comparison of two high-accuracy Al^+ optical clocks. *Phys. Rev. Lett*. **104**, 070802 (2010).
27. Brewer, S. M. et al. $^{27}Al^+$ quantum-logic clock with a systematic uncertainty below 10^{-18}. *Phys. Rev. Lett*. **123**, 033201 (2019).
28. Ushijima, I., Takamoto, M., Das, M., Ohkubo, T. & Katori, H. Cryogenic optical lattice clocks. *Nat. Photon*. **9**, 185–189 (2015).
29. Liu, L. R. et al. Molecular assembly of ground-state cooled single atoms. *Phys. Rev. X* **9**, 021039 (2019).
30. Dörscher, S. et al. Lattice-induced photon scattering in an optical lattice clock. *Phys. Rev. A* **97**, 063419 (2018).
31. Takamoto, M., Takano, T. & Katori, H. Frequency comparison of optical lattice clocks beyond the Dick limit. *Nat. Photon*. **5**, 288–292 (2011).
32. Marti, G. E. et al. Imaging optical frequencies with 100 μHz precision and 1.1 μm resolution. *Phys. Rev. Lett*. **120**, 103201 (2018).
33. Foster, G. T., Fixler, J. B., McGuirk, J. M. & Kasevich, M. A. Method of phase extraction between coupled atom interferometers using ellipse-specific fitting. *Opt. Lett*. **27**, 951 (2002).
34. Shi, C. et al. Polarizabilities of the ^{87}Sr clock transition. *Phys. Rev. A* **92**, 012516 (2015).
35. Chwalla, M. et al. Precision spectroscopy with two correlated atoms. *Appl. Phys. B* **89**, 483–488 (2007).
36. Chou, C. W., Hume, D. B., Thorpe, M. J., Wineland, D. J. & Rosenband, T. Quantum coherence between two atoms beyond $Q = 10^{15}$. *Phys. Rev. Lett*. **106**, 160801 (2011).
37. Hume, D. B. & Leibrandt, D. R. Probing beyond the laser coherence time in optical clock comparisons. *Phys. Rev. A* **93**, 032138 (2016).
38. Tan, T. R. et al. Suppressing inhomogeneous broadening in a lutetium multi-ion optical clock. *Phys. Rev. Lett*. **123**, 063201 (2019).
39. Kaufman, A. M. et al. Two-particle quantum interference in tunnel-coupled optical tweezers. *Science* **345**, 306–309 (2014).
40. Murmann, S. et al. Two fermions in a double well: exploring a fundamental building block of the Hubbard model. *Phys. Rev. Lett*. **114**, 080402 (2015).
41. Pedrozo-Peñafiel, E. et al. Entanglement-enhanced optical atomic clock. Preprint at https://arxiv.org/abs/2006.07501 (2020).
42. Covey, J. P., Madjarov, I. S., Cooper, A. & Endres, M. 2000-times repeated imaging of strontium atoms in clock-magic tweezer arrays. *Phys. Rev. Lett*. **122**, 173201 (2019).
43. Kaubruegger, R. et al. Variational spin-squeezing algorithms on programmable quantum sensors. *Phys. Rev. Lett*. **123**, 260505 (2019).
44. Kessler, E. M. et al. Heisenberg-limited atom clocks based on entangled qubits. *Phys. Rev. Lett*. **112**, 190403 (2014).
45. Zhang, G. & Song, Z. Topological characterization of extended quantum Ising models. *Phys. Rev. Lett*. **115**, 177204 (2015).
46. Savary, L. & Balents, L. Quantum spin liquids: a review. *Rep. Prog. Phys*. **80**, 016502 (2017).
47. Titum, P., Iosue, J. T., Garrison, J. R., Gorshkov, A. V. & Gong, Z.-X. Probing ground-state phase transitions through quench dynamics. *Phys. Rev. Lett*. **123**, 115701 (2019).
48. Briegel, H. J., Browne, D. E., Dür, W., Raussendorf, R. & Van den Nest, M. Measurement-based quantum computation. *Nat. Phys*. **5**, 19–26 (2009).

Methods

Hybrid potentials

Our science potential is a 2D tweezer array operating at 813 nm, a magic wavelength for the clock transition[6], whereas the auxiliary potential operates at 515 nm, where a magic-trapping condition can be achieved for the $^1S_0 \leftrightarrow {}^3P_1$ cooling transition at 689 nm via tuning of a magnetic field[9]. The power requirements at 813 nm are more demanding compared to 515 nm, owing to the roughly three times lower polarizability, a larger diffraction-limited spot size and a reduction in available laser power at this wavelength. However, critically, because the science potential is only used for the clock-interrogation stage, where shallow traps are preferable, these power constraints do not impose a limitation on atom number or state preparation.

The auxiliary potential includes a 2D tweezer array and a crossed-beam optical lattice, which provides additional confinement along the weakly confined 'axial' axis of the tweezers. Because the required confinement is the same in all axes for 3D ground-state cooling, this axial lattice greatly reduces the power requirements on the auxiliary tweezers. In our apparatus, with a numerical aperture of NA ≈ 0.68, this corresponds to a ~30-fold reduction in required optical power per tweezer. As a result, at modest optical power, we can create near-spherical traps with trap frequencies of roughly 90 kHz in all axes. By including various losses in our system and using ~4 W of total optical power, we create 320 such traps in a 16 × 20 array (see Fig. 1b, d).

Although the tweezers, and thus the radial trap frequencies, can be balanced across the entire array, there is substantial inhomogeneous broadening of the axial trap frequencies. This is due to the relatively small 25-μm waists of the lattice beams, which are comparable to the extent of the tweezer array (Extended Data Fig. 1). As mentioned in the main text, the axial cooling and handoff performance is vastly improved in a 6 × 6 region at the centre of the array, with an average phonon occupation of $\bar{n} = 0.00^{+0.06}_{-0.00}$ ($\bar{n} = 0.06^{+0.10}_{-0.06}$), compared to the array average of $\bar{n} = 0.07^{+0.14}_{-0.07}$ ($\bar{n} = 0.25 \pm 0.12$) before (after) the handoff. Owing to the modest power requirements of the lattice, the lattice waist could easily be increased in the future without sacrificing axial trap frequency, suggesting that this enhanced performance could be achieved across the entire array.

Tweezer arrays. To prepare our 2D tweezer arrays, we image two orthogonal acousto-optic deflectors (AODs) onto each other in a 4*f* configuration. Two such systems at 515 nm and 813 nm are combined on a dichroic mirror and projected via the same high-NA objective lens, which has diffraction-limited performance between 461 nm and 950 nm. The relevant parameters for the 515-nm and 813-nm tweezers are collected in Extended Data Table 1.

We space the two axes of our array differently, with spacings of 1.5 μm and 1.2 μm along the two orthogonal axes of the array, corresponding to offsets of ~5 MHz (~3 MHz) between adjacent 515-nm (813-nm) tweezers. This keeps nearby tweezers at different optical frequencies, so that any interference is time-averaged away and can be compensated for by trap balancing. For equally spaced tweezers, we observed d.c. interference fringes that cannot be removed owing to a lack of access to the appropriate degrees of freedom in trap balancing.

To balance the depths of individual tweezers, we split off a small fraction of the light before the objective, and measure the integrated intensity per tweezer using a CMOS camera. By adjusting the relative power in the different radio frequency (RF) tones applied to the crossed AODs, it is possible to balance the total optical power in each spot to within 5% of the mean, as measured on the camera. The main limitation on this balancing is a lack of fully independent control over each spot; each of the 16 + 20 = 36 RF tones has independent phase and amplitude control, however the relative phases are more or less fully constrained to avoid large voltage spikes that can cause intermodulation due to nonlinearities in the electronics that drive the tweezer system. As a result, we have only 36 degrees of freedom for balancing a tweezer array of 16 × 20 = 320 spots. Although it is possible to explicitly balance the tweezer powers at the atoms (for example, via light shifts or measurements of the trap frequency), we have not yet found this to be necessary, because the variations in trap depth are currently dominated by this lack of independent control.

Tweezer RF source. To supply the AODs used to generate our tweezers with appropriate RF signals, we use a custom field-programmable gate array (FPGA)-based frequency synthesizer. Specifically, the FPGA runs 512 direct digital synthesis cores, which are interleaved to generate 256 outputs with independently tunable frequency, phase and amplitude. These outputs control four separate 16-bit digital-to-analogue converters (DACs), which each drive one of the four AODs used in our system. This corresponds to 64 independent RF tones per AOD, where each tone has 36 bits of frequency resolution, 12 bits of phase resolution and 10 bits of amplitude resolution. We concurrently generate a set of four data points for each tone at a rate of 153.6 MHz, resulting in an overall sample rate of 614.4 million samples per second. This corresponds to a maximum usable frequency of ~250 MHz (here we operate in the range 100–200 MHz); however, the DACs interpolate between these points by a factor of 4, resulting in an overall sample rate of 2,457.6 million samples per second, which allows easy filtering of harmonics on each output. These outputs are amplified using two stages of linear RF amplifiers, with the final stage being a high-power (10 W) amplifier that delivers ~2 W (~5 W) of total RF power to each of the 515-nm (813-nm) AODs.

Axial lattice. To form the axial lattice, 515-nm light of ~300 mW is split in an interferometer that creates two parallel beams with variable spacing and controllable relative phase. These two beams are focused onto the atoms with a 30-mm achromatic doublet, so that each beam has a Gaussian $1/e^2$ radius of 25 μm at the atoms. These beams interfere to form a standing wave with wavevector normal to the tweezer plane. For the chosen beam spacing of 1.6 cm at the lens, the resulting lattice potential has a period of $\lambda_l \approx 1$ μm. We can flatten this potential relative to the tweezer array at the $\lambda_l/10$ level (see Extended Data Fig. 2 and Supplementary Information).

Experimental procedure

Our procedure for loading, ground-state cooling and imaging bosonic strontium-88 (^{88}Sr) atoms in 515-nm optical tweezers is described in ref. [9] (see Extended Data Fig. 3). Power-hungry operations such as initial loading and imaging are performed exclusively in these tweezers. We have observed that loading can be performed in even shallower tweezers with the aid of the axial lattice; however, this results in an additional background of atoms that populate other layers of the lattice. To avoid this, we opt to load directly into the tweezers to ensure loading of a single atom plane.

In this work, the axial lattice is used primarily for improved sideband cooling[8,9,49–51] in the axial direction. It is ramped on and off over 5 ms, and is shuttered for all stages of the experiment except for when performing sideband cooling. To shrink the size of the atomic wave packet and prevent loading of adjacent lattice fringes, we perform 5 ms of unresolved axial and resolved radial sideband cooling in the tweezers before ramping on the axial lattice. The improved axial confinement with the lattice on creates nearly isotropic traps with ~90 kHz trap frequencies along all axes, and further cooling in this hybrid potential brings most of the atoms (81^{+17}_{-22}%) to the 3D motional ground state. Because the polarization of the axial lattice is aligned to that of the 515-nm tweezers, we maintain the same 'magic field' conditions throughout this sequence[9].

To hand atoms between the two sets of tweezers, we ramp on the 813-nm tweezers in 5 ms with the 515-nm tweezers maintained at full depth, and then ramp the 515-nm tweezers off (see Extended Data

Fig. 3). The intensity servo for our 515-nm tweezers takes a few milliseconds to stabilize after being turned back on, which can heat atoms out of the 813-nm tweezers. To avoid this, while the 515-nm tweezers are nominally switched off we also move them away from the atoms with the AODs used to project them, and then shutter the 515-nm beam path. To reintroduce the 515-nm tweezers, we turn on the beam and let the intensity servo settle to low power, un-shutter the beam path, and finally move the tweezers back to overlap with the 813-nm array. By shuttering the beam, we ensure that there are no light shifts of the clock transition due to stray 515-nm light while the atoms are in the 813-nm tweezers. We note that although the handoff procedure can be performed with 0.0(3)% atom loss, for all clock data discussed in the main text this alignment was imperfect, resulting in an additional ~4% atom loss when handing atoms to and back from the science potential. Here, we choose not to correct this loss because it is inconsequential for clock performance; however, more careful and consistent calibration will be necessary for future works that are more sensitive to state purity.

Clock interrogation. After loading ground-state cooled atoms into the science potential, we can interrogate the clock transition. As in our previous work[6], we apply a magnetic field of 22 G to mix the $^3P_1$ state into the $^3P_0$ state, which opens the doubly forbidden $^1S_0 \leftrightarrow {}^3P_0$ transition at 698 nm (ref. [52]), at which point this transition can be driven optically. To avoid fluctuations in clock Rabi frequency due to intensity fluctuations, we opt to ramp up the clock laser intensity with the laser detuned from resonance by 125 kHz. Once the laser intensity servo settles, we can jump the detuning to near resonance for a variable time to excite atoms to the $^3P_0$ state. To detect the population excited to $^3P_0$ we apply a 'blow-away' pulse of 461-nm light resonant with the $^1S_0 \leftrightarrow {}^1P_1$ transition to remove atoms that were in the ground state. To return clock-state atoms to the ground state for readout, we drive the $^3P_0 \leftrightarrow {}^3S_1$ transition at 679 nm and the $^3P_2 \leftrightarrow {}^3S_1$ transition at 707 nm (see section 'Repumping' for additional details). The $^3S_1$ state decays to the whole ^3P_J manifold, such that eventually all clock-state atoms are pumped into the shorter-lived $^3P_1$ state and decay back to the ground state, where they can be read out during imaging. With this protocol we observe no reduction in $^3P_0$ maximal transfer fraction when using Rabi frequencies between $2\pi \times 7$ Hz and $2\pi \times 0.4$ Hz averaged across all ~150 atoms in the array (Fig. 1e).

All Rabi spectroscopy is performed in $25E_r$-deep tweezers, corresponding to 58 μW of optical power per tweezer, as measured at the atoms. These shallow traps are the primary limit on the achievable transfer fraction for all Rabi frequencies used in this work. Specifically, these depths result in a relatively high Lamb–Dicke parameter of $\eta = 0.83$, and thus increased sensitivity to residual motional excitation (see Supplementary Information). However, the benefit of using such shallow traps is that clock frequency shifts arising from spatial variation of the tweezer wavelengths should be bounded to below 50 mHz across the entire array, resulting in reduced dephasing[6]. To confirm this, we fitted the spectrum of each tweezer to extract its centre value, and measured a standard deviation in these trap-dependent clock frequencies of 39(2) mHz (Fig. 1e).

For Ramsey spectroscopy, we use a π/2-pulse time of ~50 ms for all relevant data. At short times, the frequency of the Ramsey fringes is set by the differential light shift imposed by the probe beam on the $^1S_0$ and $^3P_0$ states. At longer times, the loss of atom–laser coherence manifests as a randomized phase of the second π/2 pulse in the Ramsey sequence. This obscures Ramsey oscillations but preserves the probability of large excursions due to the persistence of atomic coherence, where atomic coherence is defined as the magnitude of the off-diagonal elements in the average single-particle density matrix, $|\bar{\rho}_{eg}|$.

Repumping. Our clock-state lifetime measurements can be confounded by the presence of atoms pumped into the $^3P_2$ state owing to Raman scattering of the trap light. These atoms are not distinguished from clock-state atoms during our normal blow-away measurement, and can lead to an artificially long inferred lifetime. To avoid this, we add an additional repumping step that depletes $^3P_2$ atoms before the blow-away by driving the $^3P_2 \leftrightarrow {}^3S_1$ transition at 707 nm. We note that because $^3S_1$ decays to $^3P_0$ with a branching ratio of ~1/9, this measurement alone is insufficient to accurately determine the population in $^3P_0$. As a result, we repeat the above measurement without repumping to measure the total $^3P_0 + {}^3P_2$ population. On the basis of these two measurements, we infer the true population in $^3P_0$, which appears in Fig. 2a.

Trap lifetime

Deep traps. We expect our trap lifetimes, particularly in deeper traps, to be limited by collisions with residual background gas. These collisions are substantially more energetic than the trap depths that we have access to, resulting in a vacuum lifetime that is effectively independent of trap depth[53]. This is confirmed via the procedure described in ref. [54], assuming that the main collision partners are room-temperature Σ-state H_2 molecules interacting via Van der Waals forces.

Based on this model, we expect clock-state atoms to have reduced trap lifetimes τ compared to ground-state atoms owing to their larger C_6 coefficient and thus larger scattering cross-section σ, because in this case $\tau \propto 1/\sigma \propto C_6^{-2/5}$. Using the known C_6 coefficients for collisions between H_2 and ^{88}Sr (ref. [55]), we calculate that the ratio between the ground- and clock-state trap lifetime (τ_g and τ_e, respectively) is $\tau_g/\tau_e = 1.10$, which agrees with results from ref. [30].

We estimate that the fractional frequency shifts due to these background collisions[56,57] are below the 10^{-19} level, suggesting that this is not a likely explanation for the increased decoherence rate reported in the main text.

Shallow traps. The source of the dramatic reduction of trap lifetime in shallow traps remains unknown; however, based on the above analysis, we rule out the effect of collisions with background gas. Other potential sources could include tunnelling, or heating induced by parametric modulation, pointing noise or scattered light.

For $6E_r$-deep tweezers with 1.2 μm spacing, we calculate a tunnelling rate of ~1 Hz between adjacent tweezers via exact diagonalization in one dimension. For image pairs in the experiment, we expect this tunnelling to manifest as correlated nearest-neighbour atom–vacancy and vacancy–atom events, where an atom tunnels from one site to an empty adjacent site, or pairs of atom–vacancy events, where an atom tunnels onto an occupied adjacent site, and both atoms are lost because of light-assisted collisions. We do not observe an excess of such events beyond what is expected owing to loss and imaging infidelity at any depth or hold time used in this work. This suggests that disorder, which we know is present on the scale of $>10^{-2}$ in trap depth, plays a critical role in pinning the atoms. Given the relevant tunnelling energies, this is not unexpected, because even in our shallowest traps disorder on the scale of 10^{-4} in trap depth is sufficient to freeze out tunnelling. Similar calculations suggest that the effect of loss due to Zener tunnelling along the gravitational axis is negligible at all depths explored in this work.

Atom loss can also arise from heating caused by a variety of mechanisms, including intensity and pointing noise from the trap laser, and scattered light. Intensity noise manifests as parametric modulation of the trap frequency, which, assuming a flat noise spectrum, results in exponential heating (measured in phonon number) with a time constant proportional to f_t^2, where f_t is the trap frequency. Similarly, pointing noise with a flat spectrum results in linear heating with a rate proportional to f_t^3 (refs. [58,59]). For comparison, the number of bound states, N, in a tweezer scales roughly as $N \propto \sqrt{U} \propto f_t$, where U is the trap depth. As such, assuming a flat noise spectrum, both these sources of loss should improve with reduced trap depth.

Whereas the intensity noise of our trapping laser is suppressed below 10 kHz via a servo, and is otherwise relatively flat over the frequencies relevant for heating, we do not expect this to be true for pointing

noise. In this case there is increased noise at lower frequencies due to mechanical resonances and acoustic noise, and there is no convenient way of removing such noise with a servo. As a result, pointing noise probably contributes to our reduced lifetimes at and below trap depths of $15E_r$ (corresponding to trap frequencies of 6.8 kHz). Other sources of trap-independent heating, such as scattered background light, can also begin to dominate as the traps become very shallow and N becomes small.

Clock-state lifetime and coherence

The $^3P_0$ clock-state lifetime is primarily limited by the loss processes described above, as well as by scattering of black-body radiation and the trapping light. Because we directly measure the $^3P_0$ population, as described in the main text, we are sensitive to all processes that remove population from this state, including transitions to the metastable $^3P_2$ state. Raman scattering of the trap light can drive such transitions, with dominant contributions from $^3P_0 \leftrightarrow {}^3P_1$ and $^3P_0 \leftrightarrow {}^3P_2$. For π-polarized trap light, these processes occur with rates of $4.98 \times 10^{-4} E_r^{-1}\,s^{-1}$ and $2.84 \times 10^{-4} E_r^{-1}\,s^{-1}$, respectively[30]. We note that whereas the ratio of these two scattering processes is polarization-dependent, their sum, with a value of $\Gamma_{12}^R = 7.82 \times 10^{-4} E_r^{-1}\,s^{-1}$, is conserved. All population driven into $^3P_1$ can be assumed to immediately decay into the ground state, whereas processes that return population in $^3P_2$ to the $^3P_0$ state are negligible. As such, to a good approximation, Γ_{12}^R can be treated as the total rate at which the population in $^3P_0$ is depleted because of Raman scattering.

Black-body radiation can off-resonantly drive transitions to the $^3D_1$ state, which decays to the ^3P_J manifold with branching ratios of $R_J^D = 59.65\%$, 38.52% and 1.82% for the $J = 0$, 1 and 2 states, respectively[30]. The dominant mechanism by which black-body radiation contributes to the decay of the $^3P_0$ state is via population that branches from $^3D_1$ into $^3P_1$ and subsequently decays into the ground state. This process occurs at a rate of $2.23 \times 10^{-3}\,s^{-1}$ (ref. [31]) at room temperature, which we call Γ_1^{BBR} (BBR, black-body radiation). The sum of these effects with the rate at which $^3P_0$ state atoms are lost from the tweezers, Γ_e^t, is in good agreement with our measured $^3P_0$ decay rate, $\Gamma_e = \Gamma_e^t + \Gamma_{12}^R + \Gamma_1^{BBR}$ (theory curve in Fig. 2a).

Given these decay rates, we can compute an expected Ramsey coherence time. Owing to the use of magic-wavelength traps, Rayleigh scattering of the trap light does not cause decoherence[30]. As a result, trap-induced scattering contributes only to decay of Ramsey contrast through the Raman scattering processes described above that remove population from the $^3P_0$ state. Unlike Rayleigh scattering of the trap light, black-body processes that drive population out of and back into the $^3P_0$ state (predominantly via $^3D_1$) can serve as an extra source of decoherence that is not directly reflected in the $^3P_0$ lifetime measurement. Including all these effects, the inferred Ramsey coherence time is:

$$\tau = \frac{2}{\Gamma_e^t + \Gamma_g^t + \Gamma_{12}^R + \Gamma_1^{BBR}\left(1 + \frac{R_0^D}{R_1^D}\right)}, \quad (1)$$

where Γ_g^t is the ground-state atom loss rate. All of these relevant rates are summarized in Extended Data Table 2. We note that because of the use of ^{88}Sr in this work, and given the strength of the magnetic fields used, the effects of spontaneous emission from the clock state are negligible in this analysis.

Clock accuracy

While a full accuracy evaluation is beyond the scope of this work, the prospects for using the tweezer platform as an absolute frequency reference are fairly good. Many of the dominant systematic effects in tweezer clocks are shared with optical lattice clocks[6], which have accuracies that are currently known at the 10^{-18} level[60]. These effects are discussed in ref. [6], including benefits and drawbacks associated with our use of a bosonic isotope of strontium (^{88}Sr).

The main additional complication in tweezer clocks is the shape of the tweezer potential itself. This yields modified expressions for the light shift[5,61] (see Supplementary Information) and can result in spatially nonuniform polarization[50,51], which further complicates these calculations. Our work provides a path towards minimizing these effects by operating with optical traps that are shallower than in any other platform. Furthermore, the ability to independently vary the depth of the traps opens up the possibility of performing measurements of the atomic polarizability and hyperpolarizability via synchronous comparisons that take advantage of the high stability demonstrated in this work. Such measurements are, in principle, only limited by QPN and thus can reach arbitrary precision with sufficient averaging time. Based on practical considerations, the prospects are good for characterizing these effects at the 10^{-19} level, which would further reduce any inaccuracy imposed by the tweezers.

The new scheme for atom preparation presented here does not have any impact on accuracy, given that the auxiliary potential can be fully extinguished during clock operation. In the case of an asynchronous comparison, the fast state preparation, long lifetimes and potential for repeated interrogation of the same atomic ensemble in tweezer clocks[5,6,42] lead to high duty cycles and thus reduced sensitivity to Dick effect noise in comparison to lattice clocks[6].

Although the above characteristics are promising, there are a few additional technical considerations that could limit the accuracy of current tweezer clocks. Whereas in optical lattice clocks, the lattice mirrors serve as a convenient and robust reference for the atom positions, such a reference does not exist in tweezer clocks owing to sensitivity to drifts in the entire tweezer rail (see below). This results in uncompensated Doppler shifts that can limit the atom–laser coherence time, and potentially accuracy, but could be addressed in our current apparatus by taking care to minimize air currents and vibrations in the tweezer system. So far, tweezer clocks have also suffered from inhomogeneous broadening due to slight variations in the optical wavelength of different tweezers[5,6], as characterized carefully in this work. This is the result of RF offsets imposed by the acousto-optic deflectors used to generate the tweezer arrays, and could readily be addressed with alternative technologies, such as spatial light modulators, that do not result in such shifts.

Atom–laser coherence

As a conservative measurement of our atom–laser coherence, we fit the measured Ramsey fringes with frequency as a fixed parameter, which yields a lifetime of 3.6(2) s (Extended Data Fig. 4). This is consistent with the value of 3.4(4) s measured in our previous work[6].

Our 698-nm clock light comes from a laser that is injection-locked with light stabilized to a cryogenic silicon reference cavity[12]. The output of this injection lock travels through a 50-m-long noise-cancelled fibre. For the Rabi spectroscopy presented here, the clock path further included ~4 m of fibre and ~50 cm of free-space path, which were un-cancelled and added phase noise to our clock light. For all remaining data, phase noise cancellation was performed using a reference mirror attached to the objective mount, which, to first order, sets the position of the tweezer array. This left only ~2 m of un-cancelled fibre in the path, but did not noticeably improve the atom–laser coherence of the system. This suggests that the atom–laser coherence could be limited by drifts of the position of the tweezer array relative to the objective due to air currents in the tweezer rail, or by other uncharacterized sources of noise in our fibre noise-cancellation system. We hope to address this shortcoming of the tweezer platform in future upgrades.

Limitations and scaling

The number of traps in this work is limited by thermal lensing in the optical rail used to project the deep 515-nm tweezers, which limits

the usable optical power in the rail to ~1.5 W. Given the optical power available at 515 and 813 nm, and the RF bandwidth of the AODs used in the tweezer rail, such a system could readily be scaled to more than 1,000 traps through more careful material selection and optical design. Moreover, the approach to scaling laid out here is generally applicable to other endeavours in quantum science, where it is useful to reduce the effects of scattering by using a far-detuned science potential while using a less far-detuned potential for fast, power-hungry stages of the experiment, which can alleviate constraints on atom number and/or laser power.

In our current apparatus, this scaling comes at the cost of relatively high atom loss incurred when imaging in 515-nm potentials[8,9] compared to the performance possible in 813-nm tweezers[6,42]. Although this is not an important issue for clock performance, it is relevant for gate- or many-body-based protocols for generating entanglement, where state purity can be critical. This could be addressed by imaging in a deep 813-nm 3D lattice, which can create tightly confining potentials more efficiently than a tweezer array. Such an approach would have the added benefit of improving our Lamb–Dicke parameter for clock spectroscopy. Given the imaging performance[6,42] and confinement available in such a potential, single-qubit rotations on the clock transition could reach fidelities in excess of 99.9% (see Supplementary Information). In this case, a 515-nm tweezer array and axial lattice would still be required to perform high-fidelity ground-state cooling via the $^1S_0 \leftrightarrow {}^3P_1$ transition, and would further be useful for performing site-resolved rearrangement in the lattice. Indeed, preliminary results of loading from a tweezer array into a 2D lattice potential at 813 nm, already integrated into our apparatus, showed that low temperatures were achievable.

Units and errors

Unless otherwise stated, all errors and numerical uncertainties in this article and its Supplementary Information denote a 1-s.d. confidence interval. When we quote a lifetime, we are typically referring to the 1/e decay time. As a frequency, the inverse of this quantity may be read as radians per second. When we explicitly refer to a Gaussian time constant, we are referring to the timescale associated with 1 s.d. of the Gaussian envelope.

Data availability

The experimental data presented in this manuscript are available from the corresponding author upon reasonable request. Source data are provided with this paper.

Code availability

The code used for analysis and simulation in this work is available from the corresponding author upon reasonable request.

49. Monroe, C. et al. Resolved-sideband raman cooling of a bound atom to the 3D zero-point energy. *Phys. Rev. Lett*. **75**, 4011–4014 (1995).
50. Kaufman, A. M., Lester, B. J. & Regal, C. A. Cooling a single atom in an optical tweezer to its quantum ground state. *Phys. Rev. X* **2**, 041014 (2012).
51. Thompson, J. D., Tiecke, T. G., Zibrov, A. S., Vuletić, V. & Lukin, M. D. Coherence and Raman sideband cooling of a single atom in an optical tweezer. *Phys. Rev. Lett*. **110**, 133001 (2013).
52. Taichenachev, A. V. et al. Magnetic field-induced spectroscopy of forbidden optical transitions with application to lattice-based optical atomic clocks. *Phys. Rev. Lett*. **96**, 083001 (2006).
53. Bali, S., O'Hara, K. M., Gehm, M. E., Granade, S. R. & Thomas, J. E. Quantum-diffractive background gas collisions in atom-trap heating and loss. *Phys. Rev. A* **60**, R29–R32 (1999).
54. Van Dongen, J. et al. Trap-depth determination from residual gas collisions. *Phys. Rev. A* **84**, 022708 (2011).
55. Mitroy, J. & Zhang, J. Y. Dispersion and polarization interactions of the strontium atom. *Mol. Phys*. **108**, 1999–2006 (2010).
56. Gibble, K. Scattering of cold-atom coherences by hot atoms: frequency shifts from background-gas collisions. *Phys. Rev. Lett*. **110**, 180802 (2013).
57. Bothwell, T. et al. JILA SrI optical lattice clock with uncertainty of 2.0×10^{-18}. *Metrologia* **56**, 065004 (2019).
58. Savard, T. A., O'Hara, K. M. & Thomas, J. E. Laser-noise-induced heating in far-off resonance optical traps. *Phys. Rev. A* **56**, R1095–R1098 (1997).
59. Gehm, M. E., O'Hara, K. M., Savard, T. A. & Thomas, J. E. Dynamics of noise-induced heating in atom traps. *Phys. Rev. A* **58**, 3914–3921 (1998).
60. Bloom, B. J. et al. An optical lattice clock with accuracy and stability at the 10^{-18} level. *Nature* **506**, 71–75 (2014).
61. Ovsiannikov, V. D., Pal'chikov, V. G., Taichenachev, A. V., Yudin, V. I. & Katori, H. Multipole, nonlinear, and anharmonic uncertainties of clocks of Sr atoms in an optical lattice. *Phys. Rev. A* **88**, 013405 (2013).
62. Safronova, M. S., Zuhrianda, Z., Safronova, U. I. & Clark, C. W. Extracting transition rates from zero-polarizability spectroscopy. *Phys. Rev. A* **92**, 040501 (2015).

Acknowledgements We acknowledge discussions with R. B. Hutson, J. K. Thompson, M. Foss-Feig, S. Kolkowitz and J. Simon. We further acknowledge F. Vietmeyer and M. O. Brown for assistance in the design and development of our FPGA-based tweezer control system. This work was supported by ARO, AFOSR, DARPA, the National Science Foundation Physics Frontier Center at JILA (1734006) and NIST. M.A.N., E.O. and N.S. acknowledge support from the NRC research associateship programme.

Author contributions A.W.Y., W.J.E., M.A.N., N.S. and A.M.K. built and operated the tweezer apparatus, and the silicon-crystal-stabilized clock laser was operated by W.R.M., D.K., E.O. and J.Y. All authors contributed to the data analysis and the development of the manuscript.

Competing interests The authors declare no competing interests.

Additional information

Supplementary information is available for this paper at https://doi.org/10.1038/s41586-020-3009-y.

Correspondence and requests for materials should be addressed to A.M.K.

Peer review information *Nature* thanks Ahmed Omran and the other, anonymous, reviewer(s) for their contribution to the peer review of this work. Peer reviewer reports are available.

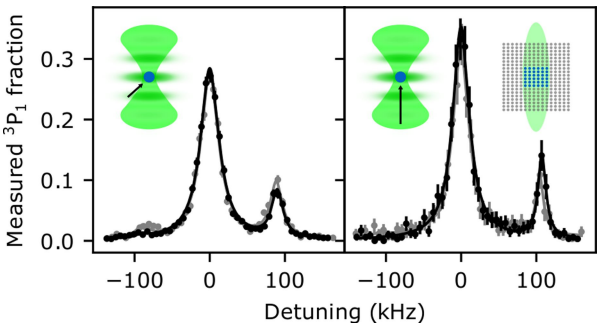

Extended Data Fig. 1 | Sideband cooling and inhomogeneous broadening. The trap frequency and cooling performance in the radial direction is uniform across the entire array, as further confirmed by spectra taken along a radial axis orthogonal to that of the data presented in Fig. 1d (left). However, in a reduced 6 × 6 region at the centre of the array (shown in the far-right inset), the axial cooling performance is vastly improved (right), with an average phonon occupation of $\bar{n} = 0.00^{+0.06}_{-0.00}$ ($\bar{n} = 0.06^{+0.10}_{-0.06}$) before (after) the handoff. This is due to the comparable extent of the lattice beams to the tweezer array (the light-green contour in the far-right inset shows the region over which the lattice intensity stays within 90% of its maximal value). Each data point corresponds to 20 repetitions of the experiment.

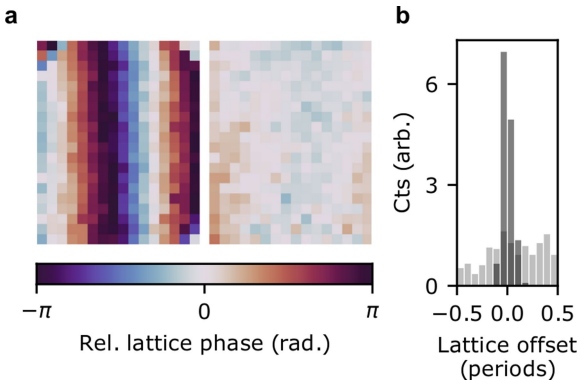

Extended Data Fig. 2 | Lattice alignment. a, **b**, Spatial phase of the standing-wave lattice at each tweezer, inferred from measurements at 15 values of the lattice phase averaged over 100 trials (see Supplementary Information) with an intentional tilt (**a**, left) and properly aligned (**a**, right). These show that it is possible flatten the lattice relative to the entire tweezer array to within 1/10 of a lattice period (**b**). This allows for high-fidelity sideband cooling in all axes. 'Cts', counts; 'arb.', arbitrary units.

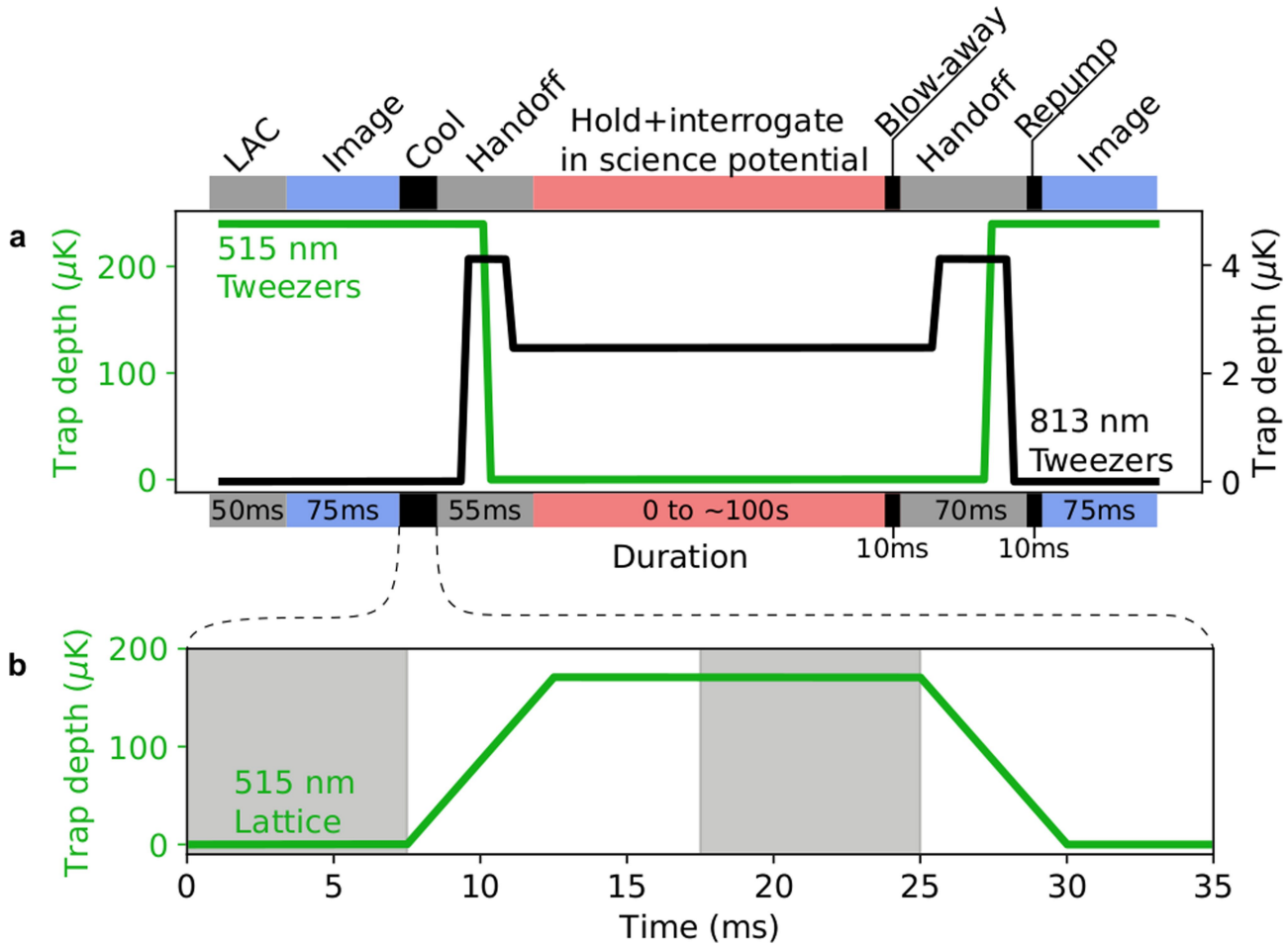

Extended Data Fig. 3 | Timing of experimental sequence. a, The green and black curves track the depths of the 515-nm and 813-nm tweezers, respectively. The coloured regions above and below the graph categorize each step of the experiment (described in more detail in Methods). We find that maintaining the 813-nm tweezers at a depth greater than $20E_r$ during the ramp down improves the fidelity of the handoff procedure. Not shown is the time required to load atoms into the 515-nm tweezers from the magneto-optical traps used for initial trapping and cooling, which takes roughly 120 ms. LAC, light-assisted collisions. **b**, Zoomed-in view of our cooling procedure, showing the depth of the axial lattice. We perform two rounds of sideband cooling, indicated by the two regions shaded in grey. The first, done before ramping up the axial lattice, does not cool axial motion to the ground state. Instead, it is important for reducing the size of the atomic wave packet to ensure loading of a single lattice fringe.

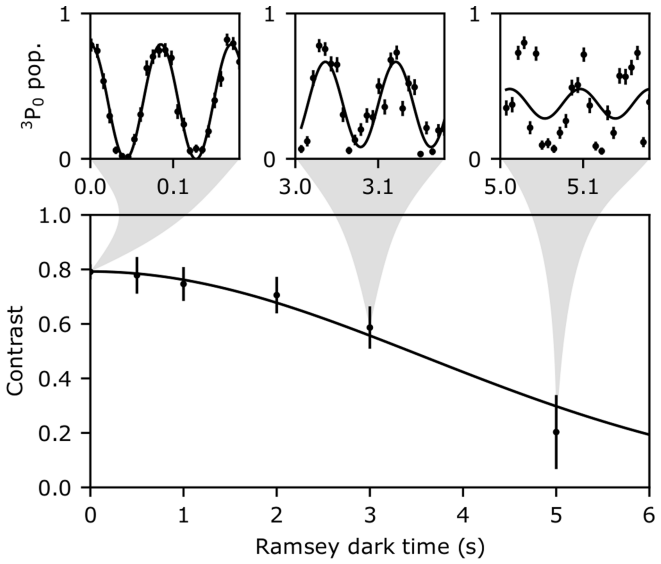

Extended Data Fig. 4 | Measuring atom–laser coherence. Fitting measured Ramsey fringes with fringes of a fixed frequency provides a conservative estimate of atom–laser coherence. Callouts share *x*-axis units with the main plot, and show the fitted Ramsey data (the same data as used in Fig. 2b). 'pop.', population.

Extended Data Table 1 | Relevant optical trapping parameters

	515 nm	813 nm
Available optical power	10 W	3 W
Ground-state polarizability, α^{E1}	900 a_0^3 [62]	280 a_0^3 [34]
Tweezer $1/e^2$ Gaussian radius	480(20) nm	740(40) nm

The higher polarizability and available laser power, as well as tighter spatial confinement, make the 515-nm tweezers more appropriate for cooling and imaging atoms in larger tweezer arrays, because these operations require more strongly confining traps. Previous data from refs. [34,62].

Extended Data Table 2 | Rates contributing to the predicted Ramsey lifetime

Values inferred from measurement (s)	
$1/\Gamma_g^t$	101(6)
$1/\Gamma_e^t$	92(5)*
$1/\Gamma_e$	43(4)
Theory values ($\times 10^{-3}$ s^{-1})	
Γ_0^{BBR} ($^3\mathrm{P}_0 \Rightarrow {}^3\mathrm{P}_0$)	$3.45(22)$ [30]
Γ_1^{BBR} ($^3\mathrm{P}_0 \Rightarrow {}^3\mathrm{P}_1$)	$2.23(14)$ [30]
Γ_2^{BBR} ($^3\mathrm{P}_0 \Rightarrow {}^3\mathrm{P}_2$)	$0.105(7)$ [30]
Γ_0^{R} ($^3\mathrm{P}_0 \Rightarrow {}^3\mathrm{P}_0$)	$0.557\ (\mathrm{U/E_r})$ [30]
Γ_{12}^{R} ($^3\mathrm{P}_0 \Rightarrow {}^3\mathrm{P}_1, {}^3\mathrm{P}_2$)	$0.782\ (\mathrm{U/E_r})$ [30]

All measured values are for a trap depth of 15E_r, based on interpolating between the nearest points in Fig. 2a. The asterisk indicates that the inferred value of Γ_e^t is dependent on the reasoning and theory values presented in Methods. Note that Γ_2^{BBR} is smaller than the error bars on the other processes, so we neglect this process in our analysis. U is the trap depth and E_r is the recoil energy of an 813-nm photon. Previous data from ref. [30].